Aeroelastic Stability of Axially Moving Webs Coupled to Incompressible Flows

Merrill Vaughan
Graduate Student Researcher

Arvind Raman
Associate Professor

Dynamic Systems and Stability Laboratory,
School of Mechanical Engineering,
Purdue University,
585 Purdue Mall,
West Lafayette, IN 47907-2088

The aeroelastic flutter of thin flexible webs severely limits their transport speeds and consequently the machine throughputs in a variety of paper, plastics, textiles, and sheet metal industries. The aeroelastic stability of such high-speed webs is investigated using an assumed mode discretization of an axially moving, uniaxially tensioned Kirchhoff plate coupled with cross and machine direction flows of a surrounding incompressible fluid. The corresponding aerodynamic potentials are computed using finite element solutions of certain mixed boundary value problems that arise in the fluid domain. In the absence of air coupling, the cross-span mode frequencies tightly cluster together, and the web flutters via mode coalescence at supercritical transport speed. Web coupling to an initially quiescent incompressible potential flow significantly reduces the web frequencies, substantially modifies the mode shapes, and separates the frequency clusters, while only marginally affecting the flutter speed and frequency. The inclusion of machine direction base flows significantly modifies the web stability and mode shapes. Cross machine direction flows lead to the flutter with vanishing frequency of very high cross-span nodal number modes, and the unstable vibration naturally localizes at the leading free edge. These results corroborate several previous experimental results in literature and are expected to guide ongoing experiments and the design of reduced flutter web handling systems. [DOI: 10.1115/1.2910902]

1 Introduction

The manufacture, processing, and use of paper, plastics, magnetic tapes, thin sheet metals, and textiles often involve high-speed transport of thin, wide continuous sheets of material known as webs. Tension is applied to the web in the direction of its transport as it travels through a series of rollers, while its edges remain unsupported. High amplitude web vibration, characterized as flutter, has been observed at the free edges. Flutter leads to poor quality products and even web breakages, causing large financial losses.

The transverse vibrations of wide axially moving media in the absence of fluid coupling have been studied through the use of prestressed moving plate models and linear and nonlinear membrane models. Ulsoy and Mote [1] used the classical Ritz discretization of a pretensioned axially moving plate to study the vibrations of wide band saw blades. Wang [2] developed a mixed finite element formulation based on the Mindlin–Reissner plate theory with transverse deflection and shear deformation included in order to predict stresses in orthotropic webs. Laukkanen [3] extended the work by Wang [2] by offering a correction to the gyroscopic inertia matrix and illustrating how waves reflect at the free edges of the web. Although normal pressures due to air loading may be implemented in the finite element method (FEM) formulations described above, the pressure loading is an input to the equations, and therefore must be assumed or known a priori. Koivurova and Pramila [4] included geometric nonlinearities in modeling the vibrations of a membrane and showed that the critical speed slightly increased upon inclusion of the nonlinearities. Mockensturm and Mote [5] investigated steady motions of translating twisted webs via a nonlinear shell theory. They showed that any degree of twist at subcritical speeds causes increased compressive stresses in the cross-web direction, increasing the likelihood of wrinkling. Raman et al. [6] modeled a continuous web supported between rollers as a thin axially moving Kirchhoff plate with small but finite bending stiffness to tension ratio. The effects of air coupling and nonuniform tension were included in the model. However, the focus of the paper was on the frequency clustering effects in paper webs, and numerical results on the fluid coupling were not presented.

The vibrations and flutter of *stationary* webs and thin films coupled to a surrounding moving fluid have been studied by a number of investigators. Guo and Paidoussis [7] investigated the stability of a rectangular plate in channel flow by modeling the plate as a beam in a potential flow. However, width dependent effects were neglected in the model. Web flutter observations in moving webs have demonstrated that flows in the cross machine direction, such as those induced by blowers in drying processes, can cause web flutter (see Hill [8] and Watanabe et al. [9]). Motivated by this observation, several researchers have studied the vibrations and stability of stationary webs with various boundary conditions and subject to a cross fluid flow. Chang and Moretti [10,11] and Chang et al. [12] modeled the web as an infinitely wide, tensioned, translating Kirchhoff plate surrounded by a potential flow with a base velocity in the cross machine direction. Chang and Moretti [11] include a translating web in the initial model but neglect the effect of transport speed in the subsequent analyses. These papers present several experiments on stationary and moving webs in a cross flow. The cross flow speed at which flutter occurs generally tended to increase with increasing tension, while the effect of the transport velocity was unclear in the range of velocities tested (0–4.88 m/s). Furthermore, the theoretical flutter speed was generally less than the measured flutter speed, but not in all cases. Watanabe et al. [9] investigated flutter due to cross flow on stationary paper sheets clamped only at the leading edge and flutter due to cross flow on stationary tensioned paper webs, covered by a fairing at the leading free edge. Thin paper sheets (0.028 mm) were noted to exhibit complicated motion that included cross flow directional modes, while thick paper (0.235 mm) exhibited a simpler motion that the authors described

Contributed by the Applied Mechanics Division of ASME for publication in the JOURNAL OF APPLIED MECHANICS. Manuscript received September 22, 2003; final manuscript received January 21, 2007; published online December 8, 2009. Review conducted by Igor Mezic.

as traveling waves moving in the flow direction. Photography of smoke streamlines demonstrated that there is no large-scale flow separation around fluttering sheets or webs. Although vortices tended to be more abundant around the thinner sheet tested, the vorticity was small in magnitude and thus the flow was largely irrotational. Watanabe et al. [13] used a beam model and estimated the unsteady lift and friction drag on a web to predict the onset of flutter due to cross flow. Their model also underpredicted the cross flow flutter speed.

The coupling of *axially moving* webs with surrounding air has for the most part been investigated using one-dimensional beam or string models along with ad hoc fluid models. Pramila [14,15] showed that the effective mass of the web is increased because of the surrounding air. In both works, the effect of the added mass on the web critical speed was investigated. The stationary fundamental frequency of the web is reduced by as much as 400% due to the added inertia effect from the air. Pramila [14,15] experimentally verified the reduced frequencies on a web moving at low subcritical speeds. Wang [16] investigated the effect of web porosity and dual sided air bearings on the traveling string with added mass model. These results demonstrated that air bearings tend to reduce the amplitude of oscillations and that web porosity has very little effect on transient response for the scenario considered.

To refine the inclusion of fluid coupling, Niemi and Pramila [17] performed a FEM analysis of the transverse vibrations of a linear membrane submerged in an initially quiescent, incompressible potential flow. The results demonstrated that the web frequencies reduce without affecting the onset of critical speed. However, a uniaxially tensioned linear membrane model is a fundamentally ill-posed mathematical problem. To overcome this problem, they introduced an artificial tensioning effect in the cross-span direction. Moreover, the web aeroelastic stability and flutter were not considered.

The present work extends the work of Raman et al. [6] to investigate in detail the effects of the fluid coupling on the vibration and stability of axially moving webs at sub- and supercritical speeds. The main contributions of the paper are (i) to model and discretize the transverse vibrations of a uniaxially tensioned, axially moving plate of finite width coupled to initially quiescent and initially moving incompressible flows, (ii) to clearly describe the effect of incompressible fluid coupling on the subcritical speed web vibration frequencies and mode shapes, (iii) to explain the effect of incompressible fluid coupling on supercritical speed flutter, flutter frequency, and flutter mode, (iv) to demonstrate that the presence of an initially axially moving flow can considerably modify the flutter speed and significantly affect the edge vibration amplitude at flutter, (v) to clearly explain the mechanism through which an initially cross machine direction flow destabilizes the web vibrations even at small flow velocities, and (vi) investigate the effects of different damping mechanisms on the analytical predictions. These results are expected to guide ongoing experiments and the design of reduced flutter web handling systems.

2 Modeling and Discretization

The rectangular web considered here is modeled as an isotropic, linearly elastic, uniaxially tensioned axially moving Kirchhoff plate. The equations of motion describing the out-of-plane vibrations of such a plate were derived by Ulsoy and Mote [1] using Hamilton's principle and are given as

$$\rho u_{,tt} + 2\rho c u_{,xt} + (\rho c^2 - N_{xx}) u_{,xx} + D\nabla^4 u + C_a u_{,t} + C_w (u_{,t} + c u_{,x}) = f \tag{1}$$

where $u(x,y,t)$ is the Eulerian description of transverse web deflection, ρ is the web mass per unit area, c is the axial web transport velocity, $D=(Eh^3)/[12(1-\mu^2)]$ is the web bending stiffness, with E, μ, and h denoting, respectively, Young's modulus, Poisson's ratio, and the thickness of the web. Additionally, ∇^4 is the biharmonic operator, N_{xx} is the uniaxial membrane tension per unit width, and f is the surface pressure. Dissipative effects are modeled through the inclusion of stationary and comoving, distributed velocity proportional damping, characterized by the constant coefficients C_a and C_w. The origin for the analysis is centered on the web, and a Cartesian vector basis $\{\mathbf{E}_1,\mathbf{E}_2,\mathbf{E}_3\}$ is fixed at the origin and aligned with the (x,y,z) coordinate system, as shown in Fig. 1. The web is free at $y=-b/2,b/2$, where b is the width of the web, and the web is assumed to be simply supported at the upstream and downstream edges, $x=-a/2,a/2$, where a is the length of the web span. Simply supported boundary conditions are assumed to be sufficiently accurate for predicting the linear vibrations of webs with small bending stiffness to tension ratio stretched across finite radius rollers [18].

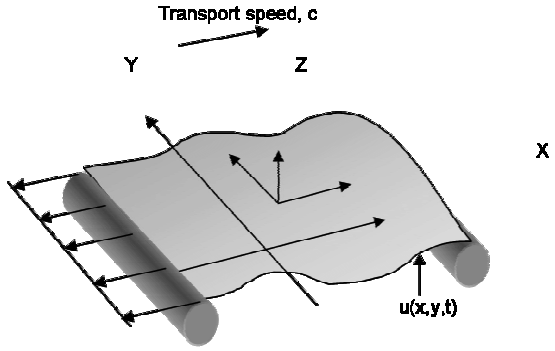

Fig. 1 A schematic depicting the translating web with uniform uniaxial tension and coupling to base fluid flows

The aerodynamic coupling of the web with an initially quiescent fluid and fluid flows with initial base flow velocities V_x and V_y is also considered. Such base flows frequently occur in web handling systems and may arise, for example, as a consequence of the three-dimensional boundary layers generated by the web motion near its free edges or from intentionally induced air flows in dryers. If $\mathbf{u}(x,y,z,t)$ is the velocity field of an inviscid, incompressible fluid, the field equations governing the balance of linear momentum and the continuity equations of the Euler fluid are given by [19]

$$\frac{\partial \mathbf{u}}{\partial t} + \mathbf{u}\cdot\nabla\mathbf{u} = -\frac{1}{\rho_{\text{air}}}\nabla p, \quad \nabla\cdot\mathbf{u} = 0 \tag{2}$$

where ρ_{air} is the air density and $p(x,y,z,t)$ is the pressure defined at every point in the fluid domain. Additionally, if the flow field is irrotational, $\mathbf{u}=-\nabla\cdot\Phi$, where $\Phi(x,y,z,t)$ is an aerodynamic potential defined at each point in the fluid domain. For the problem under consideration, let $\Phi=\phi^*+\phi$, where $\phi^*=-V_x x - V_y y$ is the steady potential associated with the steady base velocity, and $\|\phi\| \ll 1$ is a small perturbation induced by the web vibration. Substitution of this form of the aerodynamic potential into Eq. (2), linearization of the momentum equations about the steady base velocity, and upon integration of the resulting equations, the linearized Bernoulli equation and the continuity equation take the form [17,11]

$$p(x,y,z,t) = \rho_{\text{air}}\left(\frac{\partial\phi}{\partial t} + V_x\frac{\partial\phi}{\partial x} + V_y\frac{\partial\phi}{\partial y}\right), \tag{3a}$$

$$\nabla^2\phi = 0 \tag{3b}$$

Next, the velocity matching conditions between the inviscid fluid and the vibrating web are systematically derived. The time varying surface of the vibrating web is given by $F(x,y,z,t)=z-u(x,y,t)=0$. As derived by Lord Kelvin [19], for the fluid velocity to remain purely tangential to the moving surface, the material derivative of the above surface measured for any fluid particle on

the surface must vanish. This requirement can be compactly written as $DF/Dt=0$, $D(\cdot)/Dt=\partial(\cdot)/\partial t+\mathbf{u}\cdot\nabla(\cdot)$. Use of the irrotational flow assumption along with the above form of the aerodynamic potential and subsequent linearization leads to the following boundary conditions on the surface of the vibrating web:

$$-\frac{\partial\phi}{\partial z}=\frac{\partial u}{\partial t}+V_x\frac{\partial u}{\partial x}+V_y\frac{\partial u}{\partial y}\quad\text{on }\mathcal{A} \tag{4}$$

where $\mathcal{A}$ is the area of the web. Furthermore, the far field fluid boundary condition requires

$$\lim_{r\to\infty}\phi_{,n}(x,y,z,t)=0\quad\text{(far field radiation condition)} \tag{5}$$

where $r^2=x^2+y^2+z^2$ and n is the surface normal. Furthermore, the potential $\phi(x,y,z,t)$ can be written as the sum of two components, one that is symmetric with respect to the plane $z=0$ and another that is antisymmetric with respect to it. The pressure on the web $f(x,y,t)$ can be derived as the difference of aerodynamic pressure between the bottom and the upper faces of the web as

$$f(x,y,t)=2\rho_{\text{air}}[\phi_{,t}(x,y,0^+,t)+V_x\phi_{,x}(x,y,0^+,t)+V_y\phi_{,y}(x,y,0^+,t)] \tag{6}$$

where $\phi(x,y,z,t)$ henceforth refers to only to the antisymmetric part of the potential.

The formulation described above is effectively the zero-circulation solution [20] of the potential flow field. In principle, an unsteady Kutta condition is also needed to uniquely determine the circulation of the field; this can result in the generation of unsteady wakes near the leading or trailing edges of the web. In what follows, we assume that effects of the wake are negligible. This is a reasonable assumption when the surrounding fluid is initially quiescent or in flowing along the machine direction. However, wake effects may become important when the fluid flows in the cross machine direction over the free edges of the web.

The following quantities are introduced to nondimensionalize the system [6]:

$$u'=\frac{u}{a},\quad x'=\frac{x}{a},\quad y'=\frac{y}{a},\quad z'=\frac{z}{a},\quad t'=t\left(\frac{N_{xx}}{\rho}\right)^{1/2},$$

$$\kappa=\frac{b}{a},\quad D=\frac{Eh^3}{12(1-\mu^2)}$$

$$\varepsilon=\frac{D}{a^2N_{xx}},\quad \Lambda=\frac{a\rho_{\text{air}}}{\rho},\quad c'=c\left(\frac{N_{xx}}{\rho}\right)^{-1/2},$$

$$V'_{x(\text{ory})}=V_{x(\text{ory})}\left(\frac{N_{xx}}{\rho}\right)^{-1/2}$$

$$C'_{a(\text{orw})}=C_{a(\text{orw})}a(\rho N_{xx})^{-1/2},\quad \phi'=\phi\left(\frac{(N_{xx}/\rho)^{-1/2}}{a}\right) \tag{7}$$

where ε is the bending stiffness to tension ratio, κ is the web aspect ratio, and Λ is the web density parameter. The primes denote the dimensionless quantities and are dropped in the subsequent analysis. In the nondimensionalized variables, $\mathcal{A}=\{(x,y)|\ -1/2<x<1/2,-\kappa/2<y<\kappa/2\}$ is the area of the web in the span. Appending the surrounding fluid pressure to the equations of motion of a flat, translating plate [1], the equations of motion and fluid continuity equations of the surrounding incompressible fluid can be written as

$$\varepsilon\nabla^4u+u_{,tt}+2cu_{,xt}+(c^2-1)u_{,xx}+C_au_{,t}+C_w(u_{,t}+cu_{,x})$$
$$=2\Lambda[\phi_{,t}(x,y,0^+,t)+V_x\phi_{,x}(x,y,0^+,t)+V_y\phi_{,y}(x,y,0^+,t)]\quad\text{on }\mathcal{A} \tag{8a}$$

$$\nabla^2\phi=0\quad\text{in }\mathcal{R}^3\setminus\mathcal{A} \tag{8b}$$

The corresponding boundary conditions are

$$u(-1/2,y,t)=u(1/2,y,t)=0,u_{,xx}(-1/2,y,t)=u_{,xx}(1/2,y,t)$$
$$=0\quad\text{(simply supported at } x=-1/2,1/2) \tag{9a}$$

$$u_{,yy}(x,-\kappa/2,t)+\mu u_{,xx}(x,-\kappa/2,t)$$
$$=u_{,yy}(x,+\kappa/2,t)+\mu u_{,xx}(x,+\kappa/2,t)=0 \tag{9b}$$

$$u_{,yyy}(x,-\kappa/2,t)+(2-\mu)u_{,yxx}(x,-\kappa/2,t)$$
$$=u_{,yyy}(x,+\kappa/2,t)+(2-\mu)u_{,yxx}(x,+\kappa/2,t)=0$$
$$\text{(free edges at } y=-\kappa/2,\ \kappa/2) \tag{9c}$$

$$-\phi_{,z}(x,y,0^+,t)=u_{,t}+V_xu_{,x}+V_yu_{,y}$$
$$\text{on }\mathcal{A}\ (\textit{normal}\text{ velocity matching}) \tag{9d}$$

$$\phi(x,y,0,t)=0\quad\text{outside }\mathcal{A}\text{ (unbaffled web)} \tag{9e}$$

$$\lim_{r\to\infty}\phi_{,n}(x,y,z,t)=0\quad\text{(far field condition)} \tag{9f}$$

The unbaffled web assumption above allows for an exchange of fluid between the upper and the lower half spaces, thus correctly modeling the fluid motion near the free edges of the web. This leads to a mixed boundary value problem for the Laplace equation (8*b*) with the boundary conditions on $z=0$ consisting of a Neumann boundary condition on $\mathcal{A}$ and a Dirichlet boundary condition outside $\mathcal{A}$ (Eqs. (9*d*) and (9*e*)).

The equations of motion (8*a*) and (8*b*) are discretized using the assumed modes method. The mass-normalized eigenfunctions $\psi_{mn}(x,y)$ of a uniformly tensioned, undamped, stationary web ($c=0$) without aerodynamic coupling ($\Lambda=0$) are used as basis functions for the discretization of Eqs. (8*a*) and (8*b*). The discretization is performed in the configuration space formulation of the gyroscopic eigenvalue problem. Accordingly,

$$u(x,y,t)=\sum_{m=0}^{\infty}\sum_{n=0}^{\infty}q_{mn}(t)\psi_{mn}(x,y)$$

$$\psi_{mn}(x,y)=C_{mn}(\sin((m+1)\pi(x+1/2)))(\cos(\alpha_{mn}y)$$
$$+\gamma_{mn}\cosh(\alpha_{mn}y)),\quad n=0,2,\ldots$$

$$\psi_{mn}(x,y)=C_{mn}(\sin((m+1)\pi(x+1/2)))(\sin(\alpha_{mn}y)$$
$$+\gamma_{mn}\sinh(\alpha_{mn}y)),\quad n=1,3\ldots \tag{10}$$

where the basis functions $\psi_{mn}(x,y)$ possess m nodes along the x axis and n nodes along the y axis. $q_{mn}(t)$ is the generalized coordinate, C_{mn} is the amplitude of the mass-normalized basis function, and α,γ are the variables that describe the cross-span basis functions. Because the equations of motion are nondimensionalized, the basis functions, which are comparison functions for the axially moving web equations (8*a*) and (8*b*), depend only on the aspect ratio κ and Poisson's ratio μ. Note that the basis functions can be conveniently divided into those that are symmetric or antisymmetric in the cross-span direction. Next, the aerodynamic potential is also expanded as follows:

$$\Phi(x,y,z,t)=\sum_{m=0}^{\infty}\sum_{n=0}^{\infty}\{V_xA_{mn1}(t)\varphi_{mn1}(x,y,z)+V_yA_{mn2}(t)\varphi_{mn2}(x,y,z)$$
$$+A_{mn3}(t)\varphi_{mn3}(x,y,z)\}-V_xx-V_yy \tag{11}$$

Each $\varphi_{mni}(x,y,z)$ ($i=1,2,3$) is constructed so that it satisfies the Laplace equation (8*b*) ($\nabla^2\phi_{mni}=0$, $i=1,2,3$) and such that when assembled together in Eq. (11), they also satisfy the accompanying boundary conditions (9*a*)–(9*f*) for the corresponding basis

Table 1 Properties of web span used in computations, corresponding to $\kappa=1$, $\varepsilon=10^{-7}$, and $\Lambda\approx 40$

Property	a	b	h	E	μ	N_{xx}	ρ	ρ_{air}
Value	1.372	1.372	25.4	6.8	0.3	100	40	1.225
Units	m	m	μm	GPa	—	N/m	g/m^2	kg/m^3

function $\psi_{mn}(x,y)$. Note that $\Phi(x,y,z,t)$ contains three time varying components $\varphi_{mni}(x,y,z)A_{mni}(t)$, each of which satisfies a different part of the velocity matching boundary condition

$$
\begin{aligned}
&-V_x A_{mn1}(t)\varphi_{mn1,z}(x,y,0^+) = V_x q(t)\psi_{mn,x}(x,y) \quad \text{on } \mathcal{A}\\
&-V_y A_{mn2}(t)\varphi_{mn2,z}(x,y,0^+) = V_y q(t)\psi_{mn,y}(x,y) \quad \text{on } \mathcal{A}\\
&-A_{mn3}(t)\varphi_{mn3,z}(x,y,0^+) = \dot{q}(t)\psi_{mn}(x,y) \quad \text{on } \mathcal{A}\\
&\varphi_{mn1}(x,y,0) = \varphi_{mn2}(x,y,0) = \varphi_{mn3}(x,y,0) = 0 \quad \text{outside } \mathcal{A}\\
&\lim_{r^2\to\infty} \varphi_{mn1,n}(x,y,z) = \lim_{r^2\to\infty} \varphi_{mn2,n}(x,y,z) = \lim_{r^2\to\infty} \varphi_{mn3,n}(x,y,z) = 0
\end{aligned}
\tag{12}
$$

Separation of time and spatial variables in Eq. (12) leads to

$$
\begin{aligned}
&A_{mn1}(t) = A_{mn2}(t) = -q_{mn}(t), \quad A_{mn3}(t) = -\dot{q}_{mn}(t)\\
&\varphi_{mn1,z}(x,y,0^+) = \psi_{mn,x}(x,y), \varphi_{mn2,z}(x,y,0^+)\\
&\qquad = \psi_{mn,y}(x,y), \varphi_{mn3,z}(x,y,0^+) = \psi_{mn}(x,y) \quad \text{on } \mathcal{A}
\end{aligned}
\tag{13}
$$

Note that the $V_x x$ and $V_y y$ components of the expansion for $\Phi(x,y,z,t)$ in Eq. (11) are symmetric across the $z=0$ plane and do not generate a pressure difference on opposite surfaces of the web. Thus, for a given basis function mn, the pressure loading is found by substituting the time varying components of $\Phi(x,y,z,t)$ from Eq. (11) into Eq. (3*a*), yielding

$$
\begin{aligned}
f_{mn}(x,y,t) = &-2\Lambda\{\varphi_{mn3}\ddot{q}_{mn}(t) + [V_x(\varphi_{mn1}+\varphi_{mn3,x})\\
&+ V_y(\varphi_{mn2}+\varphi_{mn3,y})]\dot{q}_{mn}(t) + [V_x^2\varphi_{mn1,x} + V_y^2\varphi_{mn2,y}\\
&+ V_x V_y(\varphi_{mn1,y}+\varphi_{mn2,x})]q_{mn}(t)\} \quad \text{on } \mathcal{A}
\end{aligned}
\tag{14}
$$

For the assumed modes method, consider a N term expansion in Eqs. (10) and (11). Upon substitution of these expansions into the kinetic and strain energy expressions for the web and fluid, Lagrange's equations of motion take the form of the following discretized dynamical system:

$$
\begin{aligned}
&[\mathbf{I} + 2\Lambda\mathbf{M}_{\text{air}}]\ddot{\mathbf{q}} + [2c\mathbf{G} + 2\Lambda(V_x\mathbf{G}_{\text{air1}} + V_y\mathbf{G}_{\text{air2}}) + (C_a + C_w)\mathbf{C}_1]\dot{\mathbf{q}}\\
&\quad + [(1-c^2)\mathbf{K}_1 + \varepsilon\mathbf{K}_2 + 2\Lambda(V_x^2\mathbf{K}_{\text{air1}} + V_y^2\mathbf{K}_{\text{air2}} + V_x V_y\mathbf{K}_{\text{air3}})\\
&\quad + C_w c\mathbf{C}_2]\mathbf{q} = \mathbf{0}
\end{aligned}
\tag{15}
$$

where $\mathbf{I}$ is the $N\times N$ identity matrix, and the components of the remaining matrices are provided in the Appendix. $\mathbf{q}(t)$ is the vector of the generalized coordinates $q_{mn}(t)$ and $\mathbf{M}_{\text{air}}$ is the symmetric aerodynamic loading matrix (usually nondiagonal). $\varphi_{mni}(x,y,0^+)$ are the aerodynamic potentials at the web surface to be solved with the FEM. $\mathbf{G}$ is the skew-symmetric gyroscopic matrix arising from the transport velocity, while $\mathbf{G}_{\text{air1}}$ and $\mathbf{G}_{\text{air2}}$ are skew-symmetric gyroscopic matrices due to the fluid Coriolis acceleration terms. $\mathbf{K}_1$ is the diagonal membrane stiffness matrix. The diagonal entries of $\mathbf{K}_1$ are the squares of the natural frequencies of an equivalently tensioned string, i.e., $\pi^2, (2\pi)^2$, and so on. $\mathbf{K}_2$ is the diagonal bending stiffness matrix. $\mathbf{K}_{\text{air1}}$ and $\mathbf{K}_{\text{air2}}$ are symmetric (usually nondiagonal) negative definite stiffness matrices due to the centripetal acceleration terms containing the base fluid velocity. $\mathbf{K}_{\text{air3}}$ is also symmetric and nondiagonal. Thus, the transverse vibrations of the axially moving web coupled to surrounding incompressible flow can be compactly cast in the discretized form of a classical gyroscopic system, with symmetric stiffness, positive definite damping, and circulatory terms. However, the air coupling significantly modifies the Coriolis and centripetal acceleration components of the discretized dynamical system.

Several key parameters appear in the discretized dynamical system (Eq. (15)): Λ, c, ε, V_x, and V_y. These represent, respectively, the ratio of air density to web density, the nondimensional transport speed, the web stiffness to applied tension ratio, the nondimensional base fluid velocity in the machine direction, and the nondimensional base fluid velocity in the cross-machine direction. In what follows, first, the details of the finite element method for the computation of the aerodynamic potentials $\varphi_{mni}(x,y,z)$ and consequently of the air loading matrices above are discussed.

3 FEM Computation of Aerodynamic Potentials

The objective of the finite element discretization of the fluid domain is to evaluate the aerodynamic potentials for the six air loading matrices (Eq. (15)) of the discretized web model. The use of the stationary, undamped, in vacuo web basis functions greatly facilitates this computation. Indeed, all that remains to be computed for evaluating the six air matrices are the aerodynamic potentials $\varphi_{mn_1}(x,y,z)$, $\varphi_{mn_2}(x,y,z)$, and $\varphi_{mn_3}(x,y,z)$, as solutions of the Laplace equation in the fluid domain, generated by the oscillation of the web in its $\psi_{mn}(x,y)$ basis function and in the presence of the base flows V_x and V_y. From this, the aerodynamic potentials (and their spatial derivatives) on the surface of the web are used to conveniently evaluate the air loading matrices through Eq. (16).

Because of the inherent symmetries of the web basis functions, only one-quarter of the semi-infinite fluid domain needs to be considered in the FEM computation. Furthermore, the infinite boundary is truncated to a finite radius R. The boundary conditions on the XZ and YZ planes depend on the basis function $\psi_{mn}(x,y)$ used in the computation. Because the axis origins are centered on the web, the plane YZ is a plane of symmetry for modes that are symmetric in the in-span direction. Moreover, it is a plane of antisymmetry for modes that are antisymmetric in the in-span direction. The result is similar for the XZ plane and cross-span direction. The ANSYS steady-state thermal analysis module (for Laplace's equation) with solid 20 noded 3D brick elements was used for the computation of the aerodynamic potentials. Unless otherwise noted, all the computations in this and the following sections use realistic web properties listed in Table 1. These web properties yield the following nominal parameter values: $\kappa=1$, $\varepsilon=10^{-7}$, and $\Lambda\approx 40$. Young's modulus and Poisson's ratio are estimates for paper properties from literature (see Ref. [11]). The length, width, thickness, tension, and areal density of the web are measured properties obtained from a paper web span in a high-speed industrial printing press.

The FEM meshing of the domain needs to be sufficiently accurate to converge to the exact solution. Different fluid domain FEM meshes are designed for φ_{mn1}, φ_{mn2}, and φ_{mn3}. The components φ_{mn2} and φ_{mn3} have vanishing normal velocities along the simply supported edges, while φ_{mn1} has a nonzero normal velocity along the simply supported edge. Velocity gradients are higher near the

Table 2 Entries along the diagonal of $\mathbf{M}_{air}$ matrix as the mesh density is increased by *h*-refinement

$\mathbf{M}_{air}$ Mesh number of nodes	$\int_{\mathcal{A}} \varphi_{00_3}\psi_{00}d\mathcal{A}$	$\int_{\mathcal{A}} \varphi_{10_3}\psi_{10}d\mathcal{A}$	$\int_{\mathcal{A}} \varphi_{20_3}\psi_{20}d\mathcal{A}$	$\int_{\mathcal{A}} \varphi_{01_3}\psi_{01}d\mathcal{A}$	$\int_{\mathcal{A}} \varphi_{02_3}\psi_{02}d\mathcal{A}$
5,000	0.2366	0.1378	0.0955	0.1255	0.1101
25,000	0.2380	0.1392	0.0970	0.1270	0.1114
125,000	0.2405	0.1409	0.0984	0.1289	0.1130

web, especially at edges with nonzero velocity, necessitating the use of a very fine mesh there. Once the FEM aerodynamic potential solutions are computed, the solutions are loaded into MATLAB to take inner products with respect to the basis functions to evaluate the components of each of the six air matrices. A convergence study was also performed on the effect of the mesh density on each of the air matrices with $R=6$. Table 2 describes the variation with mesh density of the added mass matrix $\mathbf{M}_{air}$ components of the ψ_{00}, ψ_{10}, ψ_{20}, ψ_{01}, and ψ_{02} basis functions. Three different mesh densities are included in Table 2, listed by the approximate number of nodes in the mesh. For all air matrices, except the $\mathbf{K}_{air2}$ matrix, entries generated from the 25,000 node fluid domain mesh are within 5% of 125,000 node mesh. To retain a similar relative accuracy for the $\mathbf{K}_{air2}$ matrix entries involving $n=0$ basis functions, the 125,000 node mesh is used to solve for φ_{m0_2} aerodynamic potentials. The 25,000 node mesh is used for all other aerodynamic potentials in the subsequent aeroelastic stability analysis.

To analyze the effect of the finite fluid domain approximation in the FEM, a detailed analysis of the effect of the fluid domain size R on each of the air loading matrices was performed. The fluid finite element domain needs to be large enough to approximate the infinite radius domain. Table 3 describes the variation with domain size to web width ratio, R/κ, of the added mass matrix $\mathbf{M}_{air}$ components of the ψ_{00}, ψ_{10}, ψ_{20}, ψ_{01}, and ψ_{02} basis functions. To ensure accuracy, approximately 125,000 total nodes, with the mesh finer near the web edges, were used for each radius considered in this radial convergence study. The table indicates that the added mass components rapidly converge within four significant figures with increasing R/κ for ψ_{10}, ψ_{01}, ψ_{20}, and ψ_{02} basis functions. This convergence is somewhat slower for the fundamental in vacuo basis function ψ_{00}. However, this convergence is rapid for added mass components of basis functions with greater number of nodal lines. These convergence results are similar for the five other air matrices. A truncation radius R equal to five or six times the web length for $\kappa \leqslant 1$ or equal to five or six times the web width for $\kappa \geqslant 1$ is sufficient to approximate the infinite domain for all the basis functions considered. This corroborates the appropriate truncation radius R reported by Niemi and Pramila [17]. Accordingly, an appropriate R/κ ratio of 6 is used for the subsequent computation.

Finally, to benchmark the above choice of mesh density and finite domain size, the proposed FEM is used to calculate the added mass effect on an oscillating, rigid, square plate in an infinite domain, incompressible fluid. Meyerhoff [21] calculated the air loading effect for this problem by means of a dipole distribution. To compute the added mass effect using the proposed FEM, the $\mathbf{M}_{air}$ matrix diagonal entry is computed for a $\psi_{RB}=1$ basis function, which corresponds to the out-of-plane rigid body oscillatory motion of a square plate. To verify the accuracy of the proposed FEM, the added mass effect for the rigid oscillating square plate is compared for $R=1$, 2, 4, 6, and 8 to the calculations by Meyerhoff and is found to lie to within $\pm 1\%$ for all $R \geqslant 2$. This comparison is shown in Table 4.

4 Convergence Tests of the Discretized System

The number of basis functions used in the assumed modes discretization needs to be sufficient to correctly predict the stability of the web system with different parameters. The calculated system frequencies are exact at $\Lambda=c=V_x=V_y=C_a=C_w=0$ and highly accurate at low parameter values regardless of the number of basis functions used because the stationary tensioned plate mode shapes are the basis functions for the discretization. However, to correctly predict eigenvalues at supercritical speeds, more basis functions need to be included than those that are to be subsequently analyzed.

Figure 2(*a*) shows the convergence behavior for the undamped system, with respect to the number of *in-span* basis functions used, of the 00 and 10 modal frequencies at $c=1.00000270$ and the convergence behavior of the 01 and 11 modal frequencies at $c=1.00000354$, while $V_x=V_y=0$ for both cases. For the given transport speeds, the 00 and 01 modes have undergone divergence instability but are gyroscopically stabilized and they monotonically converge from below. The 10 and 11 modes have not yet undergone divergence instability and they monotonically converge from above. The approximations are poor with two in-span basis functions in the discretization but are good and change very little with four or more in-span basis functions in the discretization. Convergence behavior is similar when V_x is nonzero. Thus, to accurately predict the first two in-span modal frequencies, $m=0$

Table 3 Entries along the diagonal of $\mathbf{M}_{air}$ matrix as the truncation radius is increased.

$\mathbf{M}_{air}$ R/κ	$\int_{\mathcal{A}} \varphi_{00_3}\psi_{00}d\mathcal{A}$	$\int_{\mathcal{A}} \varphi_{10_3}\psi_{10}d\mathcal{A}$	$\int_{\mathcal{A}} \varphi_{20_3}\psi_{20}d\mathcal{A}$	$\int_{\mathcal{A}} \varphi_{01_3}\psi_{01}d\mathcal{A}$	$\int_{\mathcal{A}} \varphi_{02_3}\psi_{02}d\mathcal{A}$
$R=1$	0.2598	0.1420	0.0992	0.1301	0.1146
$R=2$	0.2426	0.1410	0.0984	0.1290	0.1131
$R=4$	0.2407	0.1410	0.0984	0.1290	0.1130
$R=6$	0.2405	0.1409	0.0984	0.1289	0.1130
$R=8$	0.2404	0.1409	0.0984	0.1289	0.1129

Table 4 $\mathbf{M}_{air}$ entries from the FEM for a rigidly oscillating square plate in an infinite domain, incompressible fluid, compared to dipole distribution computation by Meyerhoff [20]. The equivalent nondimensional term for the comparison to Meyerhoff is $\pi\kappa^2 J(\kappa)/4$.

$\mathbf{M}_{air}$ R/κ	$\int_{\mathcal{A}} \varphi_{RB_3} \psi_{RB} d\mathcal{A}$ where $\psi_{RB}=1$
$R=1$	0.2460
$R=2$	0.2286
$R=4$	0.2271
$R=6$	0.2267
$R=8$	0.2265
Meyerhoff	0.2274

and $m=1$, at least four in-span basis functions are needed. This can be generalized to the use of $2(m+1)$ in-span basis functions to predict the mth and lower in-span modal frequencies. Increasing the number of cross-span basis functions per in-span basis function has little effect on the system convergence if $V_y=0$. Therefore, the results in the paper for the web system with $V_y=0$ are generated using six in-span basis functions with eight cross-span basis functions each in the discretization, a total of 48 basis functions, with only the first few in-span basis functions considered ($m \leqslant 2$) in the subsequent analysis.

Figure 2(*b*) shows the convergence behavior of the undamped system, with respect to the number of *cross-span* basis functions used, of the lowest two modal frequencies at $V_y=0.0686$ and $c=V_x=0$, with an artificially high bending stiffness to tension ratio $\varepsilon=5\times10^{-6}$. For these system parameters, none of the modes have diverged. Each modal frequency monotonically converges from above. At $\varepsilon=5\times10^{-6}$, at least 22–24 cross-span basis functions need to be used to predict the two lowest frequencies near the first critical cross flow speed. Therefore, to analyze the $\Lambda\neq0$, $c=0$, $V_x=0$, $V_y\neq0$ case, one in-span basis function with 30 cross-span basis functions is used for the discretization, and the lowest ten cross-span modes ($n \leqslant 9$) analyzed in the ensuing results.

5 Aeroelastic Stability of Undamped Webs

The effects of fluid coupling on undamped web vibration and stability are now discussed in the following order: First, the coupling of a stationary web with an initially quiescent fluid is considered; second, a moving web in an initially quiescent fluid is discussed; followed by the effects of initial machine and cross machine direction flows. The effects of dissipation will be discussed in Sec. 6.

5.1 Stationary Web Coupled to an Initially Quiescent Fluid ($\Lambda\neq0, c=V_x=V_y=0$). The aerodynamic potential generated by a given basis function of web vibration reveals several unusual features of the flow induced by the vibrating web. Figure 3(*a*) shows a contour plot at $z=0$ of the 00 basis function (in vacuo stationary web mode shape) and Fig. 3(*b*) shows the corresponding φ_{00_3} aerodynamic potential computed in ANSYS that is developed on the web surface. Symmetry and antisymmetry in the basis functions with respect to the X and Y axes are preserved in the corresponding aerodynamic potential. Furthermore, a contour plot of the φ_{00_3} aerodynamic potential at $X=0$ (see Fig. 3(*c*)) shows that the contour lines are close together near the free edges of the web ($Y=-1/2, 1/2$; $Z=0$), indicating that the fluid velocity and its gradient with respect to Y are high in the neighborhood of the free edges. The high fluid velocity gradients near the free edge underscore the importance of fine mesh refinement near the free edge of the web. Furthermore, the FEM computations clearly demonstrate that fluid mass transport occurs from above to below the web and vice versa near the web edges. This important effect

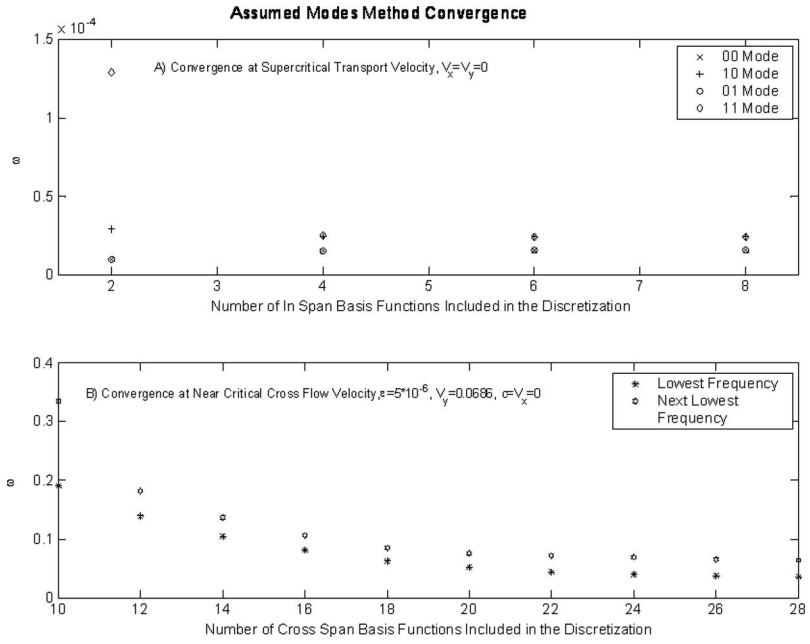

Fig. 2 Convergence of modal frequencies with respect to the number of basis functions used in the discretization. (*a*) Four cross-span modes are included as the number of in-span modes is varied. Symmetric cross-span modes 00 (×) and 10 (+) are calculated at $c=1.0000027$ and antisymmetric cross-span modes 01 (○) and 11 (◇) are calculated at $c=1.00000354$. (*b*) One in-span mode is included as the number of cross-span modes is varied at $V_y=0.0686$ near divergence instability.

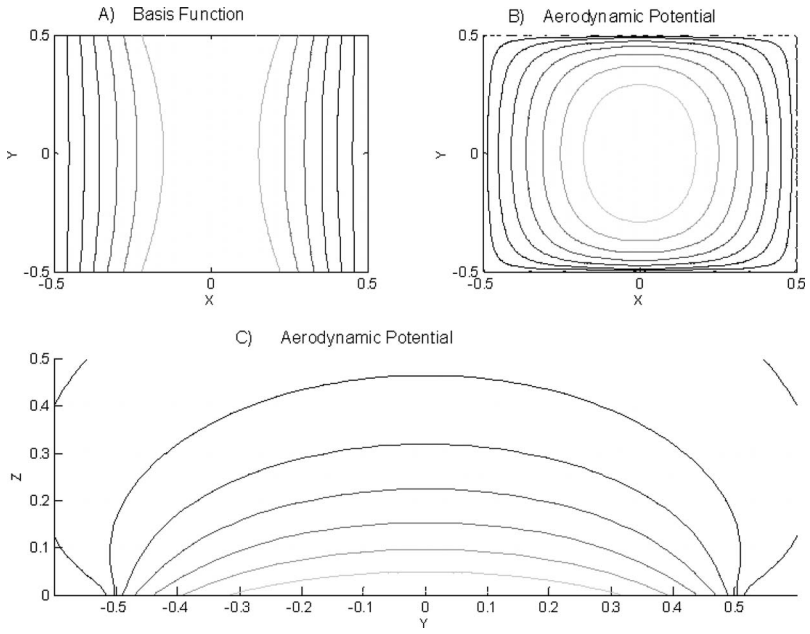

Fig. 3 (*a*) Contour plot of mass-normalized ψ_{00} basis function, (*b*) corresponding aerodynamic potential generated on the web surface, $z=0$, and (*c*) corresponding aerodynamic potential generated at $x=0$

is ignored by a baffled web assumption.

In the absence of air coupling, the web vibration frequencies are tightly clustered together around those of an equivalently tensioned string. Dimensionless natural frequencies of first four symmetric and antisymmetric cross-span modes corresponding to each $m=0,1,2,3$ (32 total) as a function of ε are shown in Fig. 4. At $\varepsilon=10^{-7}$, the bending stiffness to tension ratio of the paper web span in Table 1, at least eight cross-span modes, is tightly clustered within 0.1% of the corresponding frequencies of a taut string. Frequency clustering in very flexible in vacuo webs is manifested in a multitude of cross-span modes with nearly identical frequencies. For a fixed ε, the greater the m (nodes on the x axis), the tighter the frequencies cluster.

However, the addition of the incompressible flow coupling greatly reduces the web vibration frequencies and separates frequencies within a cluster (see Fig. 5). The reduction in frequency is most dramatic in the 00 mode with the stationary air-coupled 00 modal frequency equal to 21% of the uncoupled frequency at $\Lambda=40$. As m (nodes on the x axis) or n (nodes on the y axis) increases, the percentage reduction in the magnitude of the modal frequency decreases. The stationary air-coupled 10 modal frequency is reduced to 27% of the uncoupled 10 modal value at

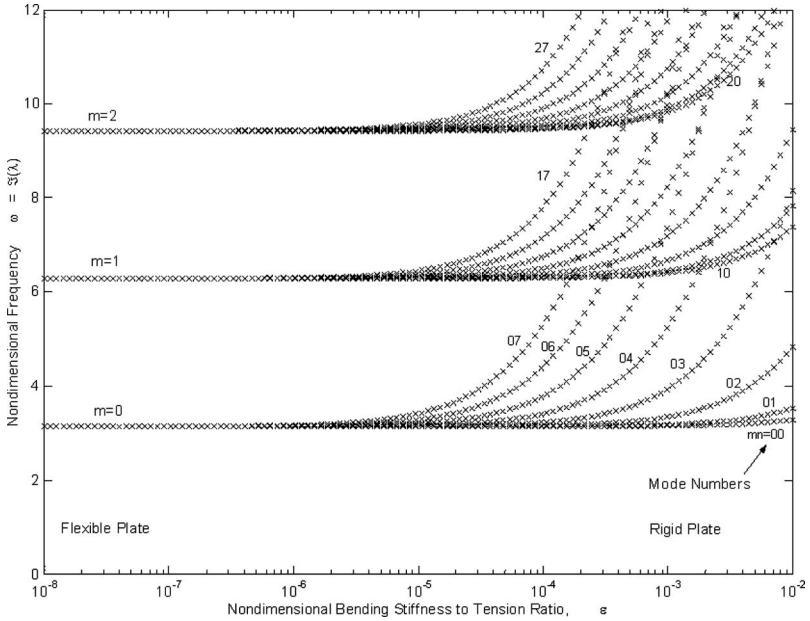

Fig. 4 Frequency clustering of a stationary, uniformly tensioned, aerodynamically uncoupled web as a function of web stiffness to tension ratio ε

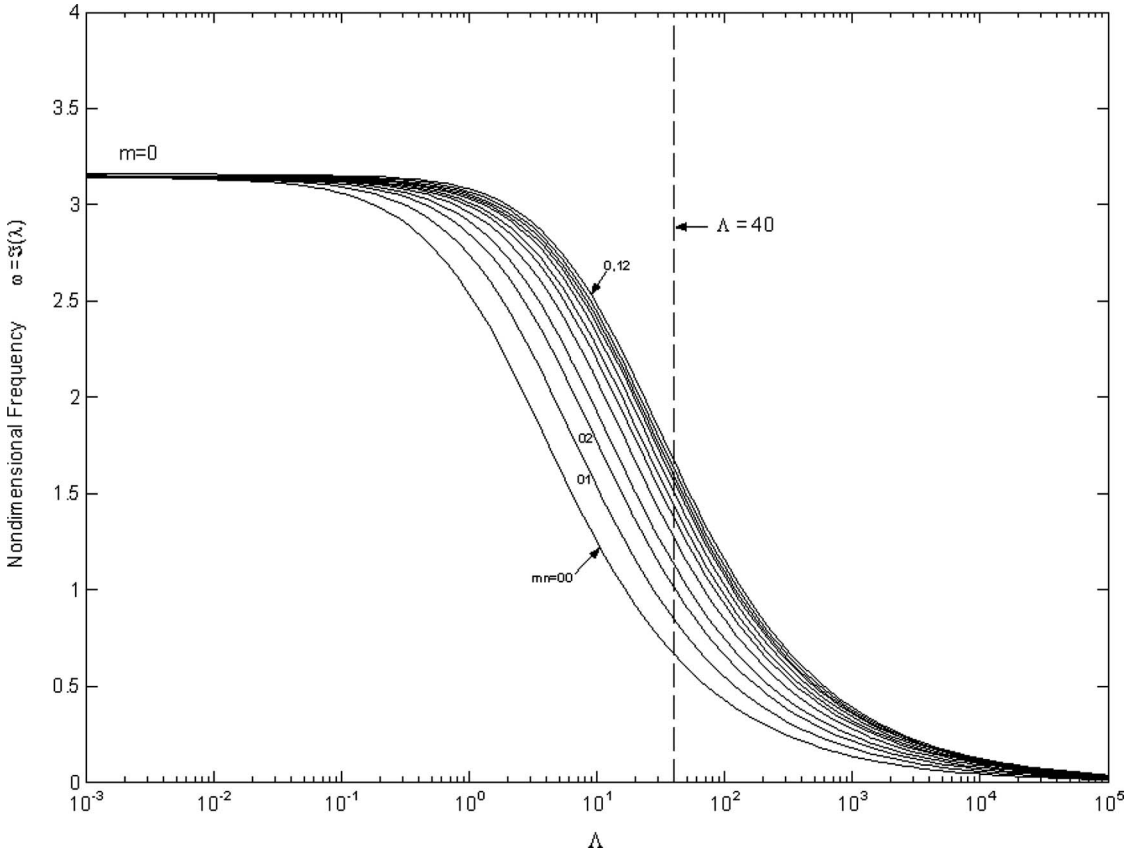

Fig. 5 Modal frequencies of the $m=0$ cluster versus Λ. $\Lambda=40$ corresponds to the web system considered in this paper.

$\Lambda=40$, and the 12 mode frequency is reduced to 34% of its uncoupled value. As Λ approaches infinity, all the modal frequencies in a cluster approach zero.

The vibration mode shapes are significantly altered by the addition of an initially quiescent potential flow. Recall that the stationary, in vacuo modes achieve their maximum amplitudes at the free edges (see Figs. 6(*a*), 6(*c*), and 6(*e*)). However, the addition of the coupling to the initially quiescent fluid significantly reduces the displacement at the free edges (see Figs. 6(*b*), 6(*d*), and 6(*f*)). A possible explanation of this result is that the web easily deflects at the free edges, so that the added fluid inertia has a more pronounced effect at the free edges than at the center of the web.

Lastly, when $c=V_x=V_y=0$, the discretized dynamical system (Eq. (15)) is a nongyroscopic, conservative system with real eigenvectors. During the free vibration of the web in any given mode, all points on the web simultaneously pass through their equilibrium position. This is not true for all the subsequent cases discussed in the paper where the presence of gyroscopic terms renders the eigenfunctions complex. In what follows, if $\mathbf{u}_k$ is the kth complex eigenvector of the discretized dynamical system (Eq. (15)), the free vibrations of the web in its kth mode are plotted as a function of time through the relation $u(x,y,t)=\mathrm{Re}(\boldsymbol{\Psi}(x,y)^T\mathbf{u}_k e^{i\omega_k t})$, where $\boldsymbol{\Psi}(x,y)$ is the vector containing the basis functions $\psi_{mn}(x,y)$.

5.2 Axially Moving Web Coupled to an Initially Quiescent Fluid ($\Lambda\neq 0$, $c\neq 0$, $V_x=V_y=0$). The coupling of an initially quiescent incompressible fluid to the axially moving web generally reduces the web vibration frequencies at subcritical speeds. Variation of the modal frequencies with respect to nondimensional transport speed, for subcritical speeds, is shown in Fig. 7. For both the in vacuo (see Fig. 7(*a*)) and in the air-coupled cases (see Fig. 7(*b*)), modes from several clusters approach zero at $c=1$. As predicted for the stationary webs, the air coupling significantly decreases the web vibration frequencies and spreads apart the clustered frequencies of the in vacuo web.

Consider now the supercritical stability of the in vacuo moving web (Figs. 8(*a*) and 8(*c*)). At the first critical transport speed, the 00 mode undergoes divergence instability. As the transport speed is increased, the 00 mode gyroscopically restabilizes until it coalesces with the 10 mode and the system undergoes coupled mode flutter. Both the 00 and 10 modes are symmetric cross-span modes. This sequence is similar for the antisymmetric cross-span modes although at slightly higher transport speeds. As the transport speed increases, more modes from different mode clusters diverge, coalesce, and flutter (see Figs. 8(*a*) and 8(*c*)). Such behavior has been previously observed for axially moving bands [1]; however, for the moving web, this cascade of mode divergences, restabilizations, and coalescence occurs over a very small supercritical speed range.

Aerodynamic coupling only slightly affects the supercritical speed stability. For the nominal $\Lambda=40$, there is very little change in the supercritical flutter speed and frequency from the in vacuo case. Figures 8(*b*) and 8(*d*) show the system eigenvalues for $\Lambda=40{,}000$, an artificially high air coupling factor. The system critical transport speeds remain unchanged from the in vacuo case as do the speeds of gyroscopic restabilization. The flutter speeds and frequencies, however, are slightly lower compared to the in vacuo case. This reduction in the flutter frequencies and flutter onset speeds is more pronounced in the higher modes, as can be seen by comparing the 20 and 21 modes in Figs. 8(*a*) and 8(*b*). Figure 9 shows the web oscillating in its 00 mode at $c=1.00000272$, a nondimensional transport speed near the first onset of flutter, at nine different time instances during 1 cycle of oscillation. Maximum displacement during the oscillation occurs at the free edge. The skew-symmetric gyroscopic matrix $\mathbf{G}$, which arises from the

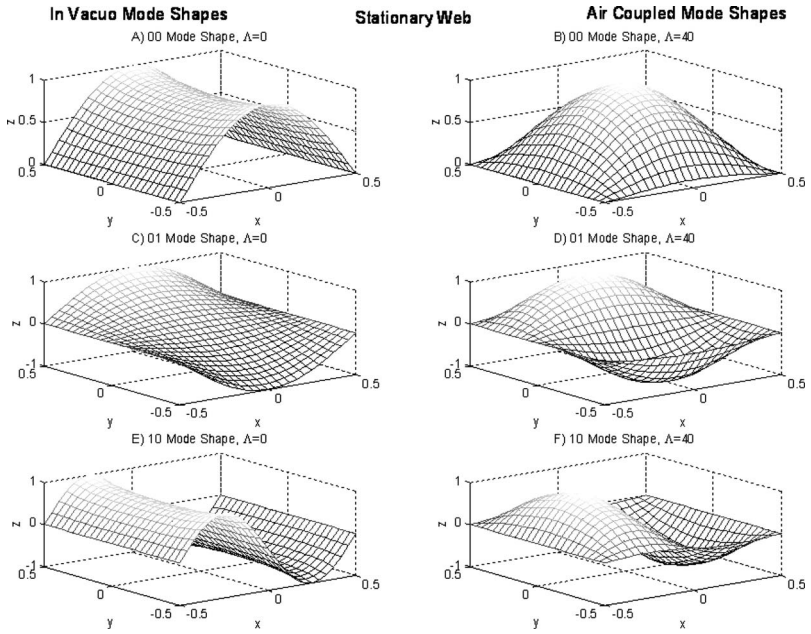

Fig. 6 Eigenfunctions of the stationary web system. (*a*) 00 mode shape at $\Lambda=0$. (*b*) 00 mode shape at $\Lambda=40$. (*c*) 01 mode shape at $\Lambda=0$. (*d*) 01 mode shape at $\Lambda=40$. (*e*) 10 mode shape at $\Lambda=0$. (*f*) 10 mode shape at $\Lambda=40$. The mode shapes are normalized in this graph such that the maximum amplitude is set to 1.

nonzero transport speed, causes downstream phase propagation in every mode shape. All points on the web no longer pass through equilibrium at the same time. Note also that the 00 mode shape resembles the 10 mode shape at this transport speed, and the two modes will coalesce at $c=1.00000273$ and flutter.

The effect of the fluid to the web density ratio parameter Λ on the supercritical speed web stability is demonstrated in Fig. 10. While critical speeds and the speed of gyroscopic stabilization remain unchanged with Λ, the flutter speed and frequency decrease as Λ increases until a threshold value of Λ. At this threshold Λ value the flutter speed coincides with the speed at which the mode was gyroscopically stabilized, the flutter frequency vanishes. As Λ is increased beyond this threshold, the mode does not gyroscopically stabilize and the web remains buckled beyond its critical speed. For the web parameters listed in Table 1, these

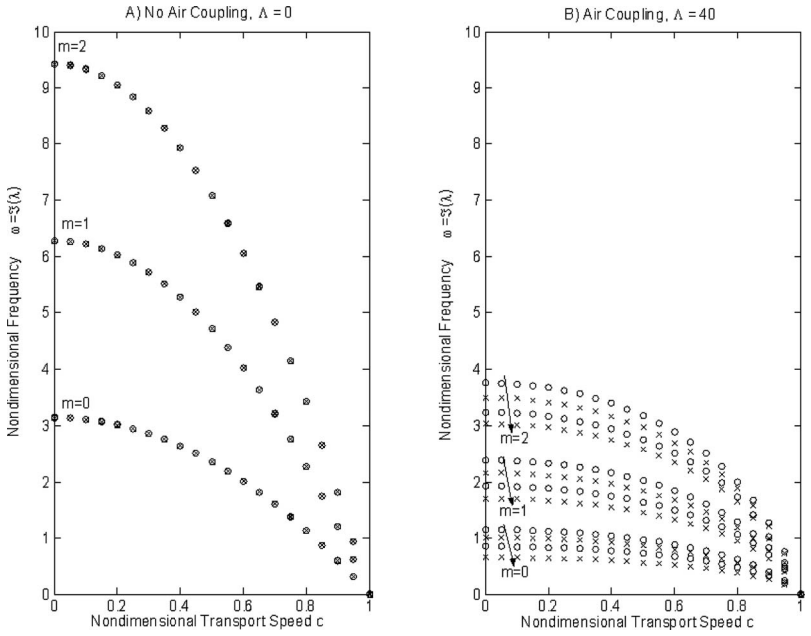

Fig. 7 (*a*) Modal frequencies of the in vacuo ($\Lambda=0$) web system versus nondimensional transport speed. (*b*) Modal frequencies of the incompressible air-coupled ($\Lambda=40$) web system. For both plots: symmetric cross-span modes (×) and antisymmetric cross-span modes (○).

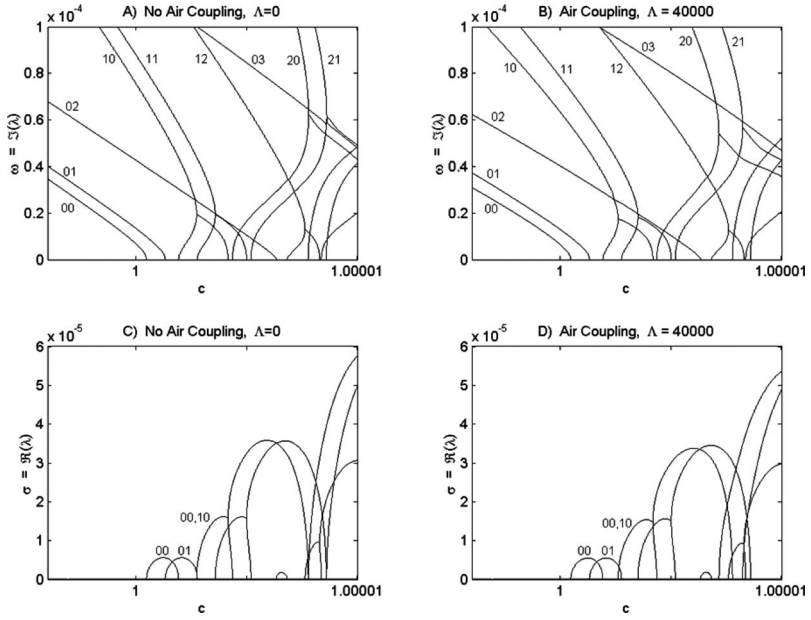

Fig. 8 Eigenvalues of the web system just before, at, and after the nondimensional critical transport speed: (*a*) imaginary part of in vacuo ($\Lambda=0$) web system eigenvalues, (*b*) imaginary part of incompressible air-coupled ($\Lambda=40{,}000$) web system eigenvalues, (*c*) real part of in vacuo ($\Lambda=0$) web system eigenvalues, and (*d*) real part of incompressible air-coupled ($\Lambda=40000$) web system eigenvalues. Mode numbers are labeled on the plot.

threshold Λ values for the 00, 10, and the 01,11 modes occur at very large Λ that may be more representative of very light webs moving in denser fluids.

5.3 Axially Moving Web Coupled to Machine Direction Base Flow ($\Lambda\neq0$, $c\neq0$, $V_x\neq0$, $V_y=0$). Inclusion of an initially axially moving base flow V_x significantly modifies web stability and modes. To systematically investigate this effect, the coupling of the machine direction flow with a stationary web is considered first. The variation with flow velocity V_x of the real and imaginary parts of the system eigenvalues is plotted for a stationary web in Fig. 11. At a flow speed $V_x=0.2806$, the 00 mode diverges first, followed by the 01 mode at a flow speed of $V_x=0.3193$. At slightly higher flow speeds, the 00 mode gyroscopically stabilizes and coalesces with the 10 mode leading to coupled mode flutter at a flow speed $V_x=0.3518$. Interestingly, the phenomena of aeroelastic divergence instability followed by gyroscopic stabilization fundamentally arise from Coriolis and centripetal acceleration terms due to the base flow and not from web transport. The

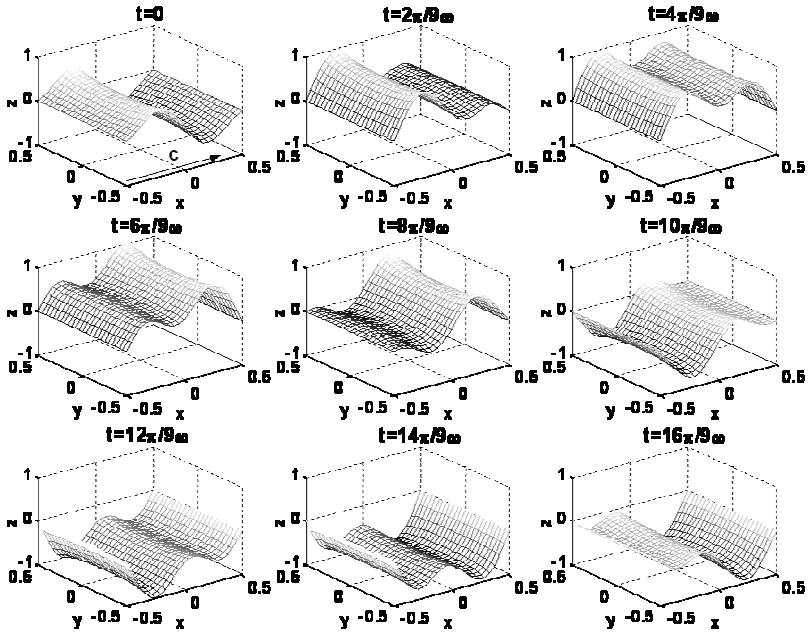

Fig. 9 First flutter mode shape for $\Lambda=40$, *c* nonzero, $V_x=V_y=0$. Nine time instances during 1 cycle of oscillation are shown.

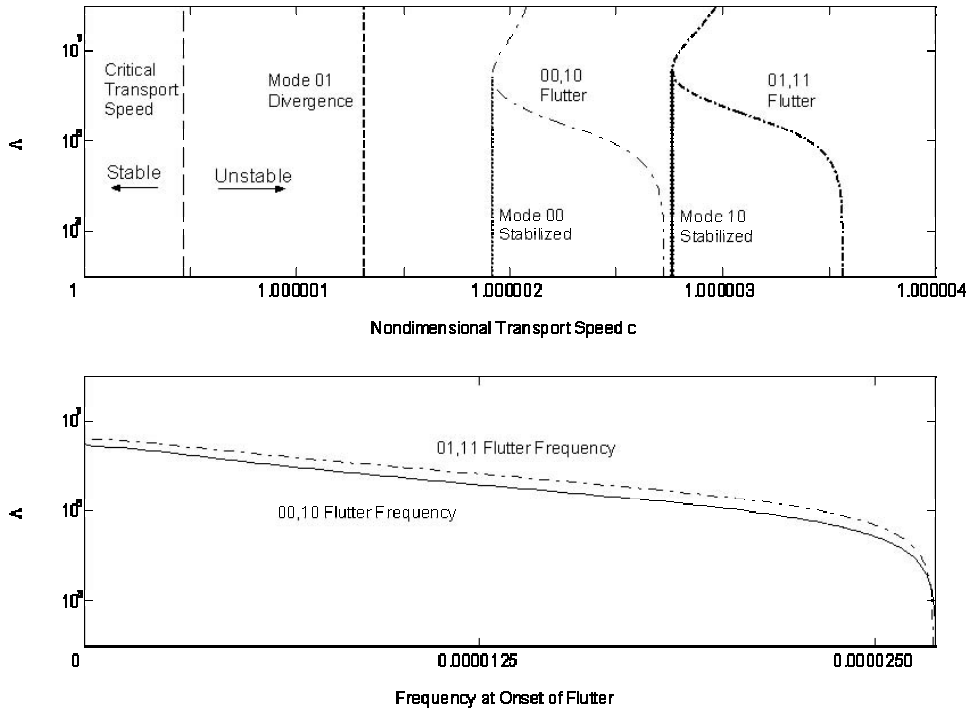

Fig. 10 (*a*) **Variation in critical transport speed, transport speed of gyroscopic stabilization, and flutter versus and Λ (*b*) variation in modal frequency at the onset of flutter versus Λ**

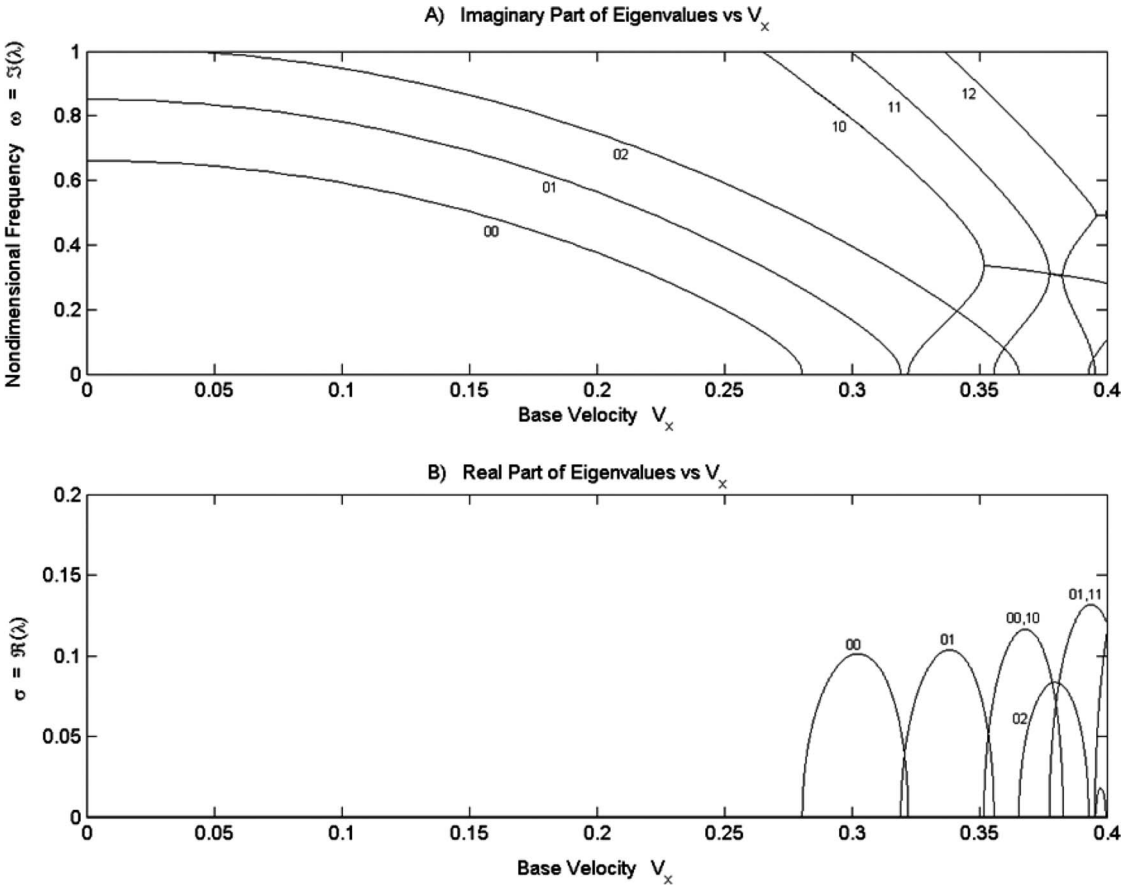

Fig. 11 Eigenvalues of the stationary web system versus fluid axial flow velocity; (*a*) imaginary part of eigenvalues and (*b*) real part of eigenvalues. Mode numbers are labeled on both plots.

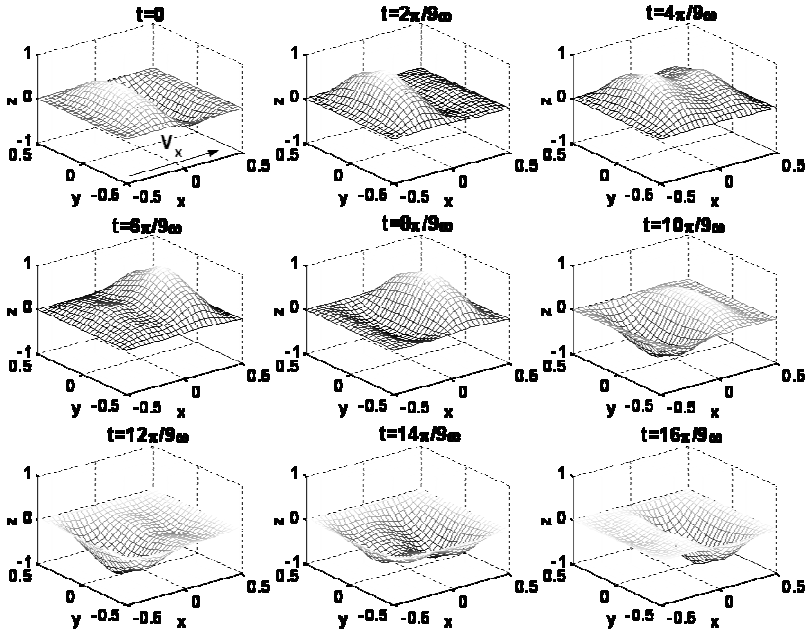

Fig. 12 First flutter mode shape for $\Lambda=40$, $c=V_y=0$, V_x nonzero. Nine time instances during 1 cycle of oscillation are shown.

first flutter mode oscillations of a stationary web coupled to an initially axially moving flow V_x are shown in Fig. 12 at nine different time instants at $V_x=0.3519$. While the flutter mode in this case is similar to the flutter mode for webs moving in quiescent fluids, the displacements at the free edges are greatly reduced in comparison to Fig. 9.

The combined effect of machine direction air flow and web transport speed on the stability boundaries is plotted in Fig. 13. In the presence of machine direction air flow, the web diverges and flutters through mode coalescence at lower transport speeds than for the $V_x=0$ case. In general for this case, transition to instability occurs first through the divergence of the 00 mode, followed by the 01 mode divergence, followed by the gyroscopic stabilization of the 00 mode, followed by flutter through mode coalescence of the 00 and 10 modes. The divergence and flutter speeds also decrease on inclusion of a machine direction flow.

The effects of flow reversal, $V_x \rightarrow -V_x$, on the web stability are also easily deduced from the discretized model. The critical speeds for divergence instability remain unchanged upon flow reversal since the overall system *stiffness* is controlled through flow centripetal acceleration terms containing V_x^2. However, flow rever-

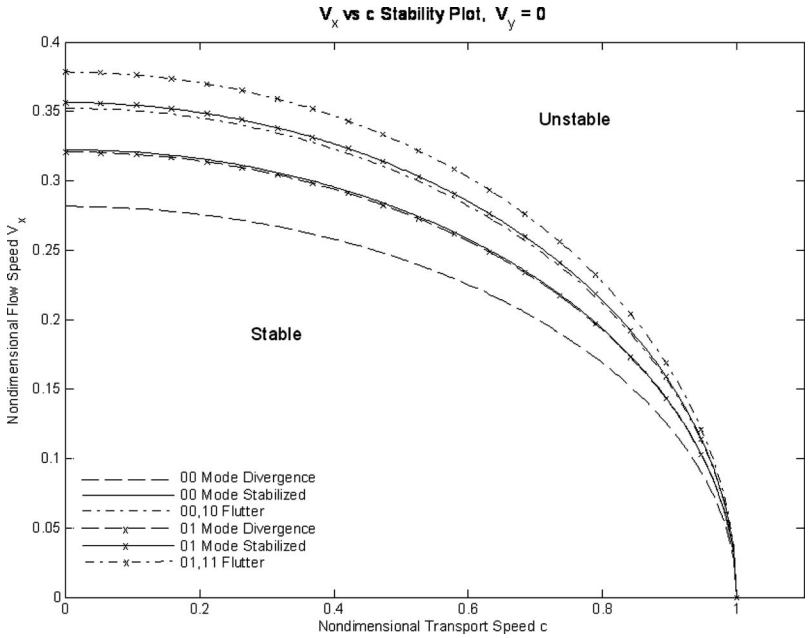

Fig. 13 First occurrences of 00 mode divergence; 00 mode gyroscopic restabilization; 00,10 modal coalescence and flutter, 01 mode divergence; 01 mode gyroscopic restabilization; and 01,11 modal coalescence and flutter for $\Lambda=40$, $c=V_y=0$, V_x nonzero

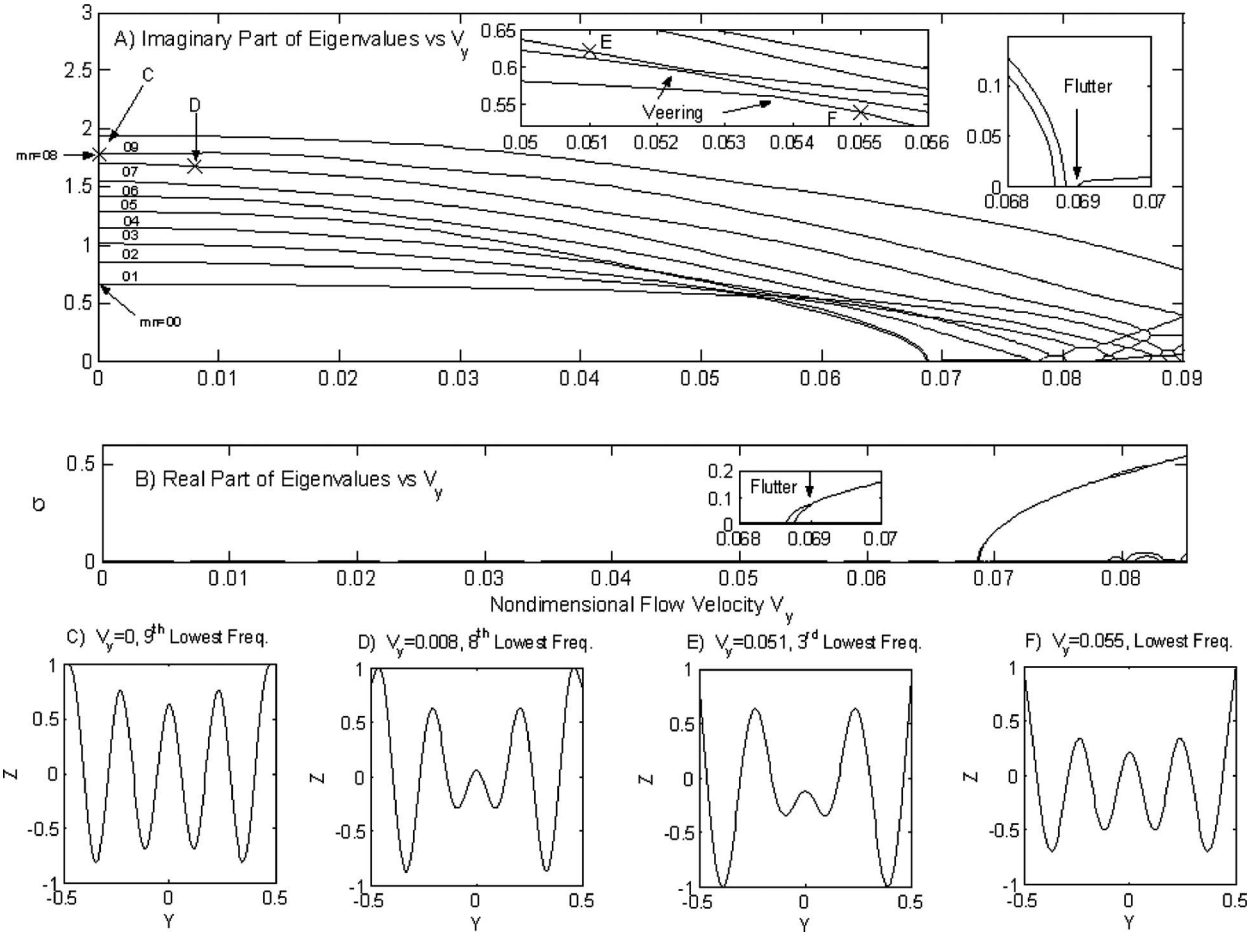

Fig. 14 Eigenvalues and eigenfunctions of the stationary web versus fluid cross flow velocity at an artificially high bending stiffness to tension ratio $\varepsilon=5\times10^{-6}$; (*a*) imaginary part of eigenvalues, (*b*) real part of eigenvalues, (*c*) eigenfunction of the ninth lowest frequency at $V_y=0$, (*d*) eigenfunction of the eight lowest frequency at $V_y=0.008$, (*e*) eigenfunction of the third lowest frequency at $V_y=0.051$, and (*f*) eigenfunction of the lowest frequency at $V_y=0.055$. Mode numbers are labeled on plot (*a*).

sal clearly affects the *gyroscopic* terms in the discretized dynamical system (Eq. (15)). Consequently, it is numerically found that following gyroscopic restabilization, flutter occurs at lower flow speeds for a given web transport speed if the flow is opposite in direction to web transport. Furthermore, the downstream phase propagation of the fluttering mode is altered upon flow reversal.

5.4 Axially MovingWeb Coupled to Cross-Machine Direction ($\Lambda\neq0$, $c\neq0$, $V_x=0$, $V_y\neq0$). To investigate the effect of a cross machine direction base flow on the web stability, the effect of the air flow on a stationary web is discussed first. For the chosen web system properties listed in Table 1 with $\varepsilon=10^{-7}$, initial computations indicated that the first unstable mode corresponds to a very high nodal number cross-span mode. However, a systematic study of the variation of eigenvalues of such high nodal number modes requires the use of prohibitively large number of cross-span basis functions for satisfactory convergence of the assumed mode method. Consequently, the computations are instead performed for a web with slightly larger bending stiffness with $\varepsilon=5\times10^{-6}$. The variation of the eigenvalues and some eigenfunctions of the stationary web as a function of the nondimensional cross flow velocity V_y is shown in Fig. 14.

Several unusual features distinguish the web instability mechanism arising from cross-machine direction air flow. First, in all the previous instability mechanisms studied, the 00 mode is typically the first to destabilize, but such is not the case here. Cross-span modes with a large number of nodal lines in the y direction (higher order modes) lose stability first. This behavior is explained by examining the components of the overall stiffness matrix $\mathbf{K}_1+\varepsilon\mathbf{K}_2+2\Lambda V_y^2\mathbf{K}_{air2}$ (see Eq. (15)). The stiffness matrix will lose positive definiteness for sufficiently large V_y through the fluid centripetal acceleration effects contained in the $2\Lambda V_y^2\mathbf{K}_{air2}$ matrix. The diagonal entries of this matrix, which are all negative, increase in magnitude as the number of nodes in the corresponding cross-span basis function increases. Thus, higher order cross-span mode frequencies more rapidly decrease with cross-flow speed than the lower order cross-span mode frequencies. However, the higher order cross-span modes have also a higher frequency at zero cross-flow speed ($V_y=0$). For small values of ε characteristic of web systems, the separation between higher order and lower order mode frequencies at zero flow speed is small, so some higher order cross-span modes diverge at lower flow speeds than the 00 mode. For the parameters considered here, the 08 dominated mode diverges first, followed closely by the 09 dominated mode.

Second, all cross-span basis functions are coupled in the presence of cross-span flow. This coupling arises through the $2\Lambda V_y\mathbf{G}_{air2}$ nondiagonal gyroscopic matrix and through the nondiagonal $2\Lambda V_y^2\mathbf{K}_{air2}$ component of the stiffness matrix. This introduces the possibility of eigenvalue veering with respect to the parameter V_y. The eigenvalues corresponding to the 07 and 08 basis functions at $V_y=0$ veer away from each other at low cross flow velocities. The corresponding eigenfunctions are "ex-

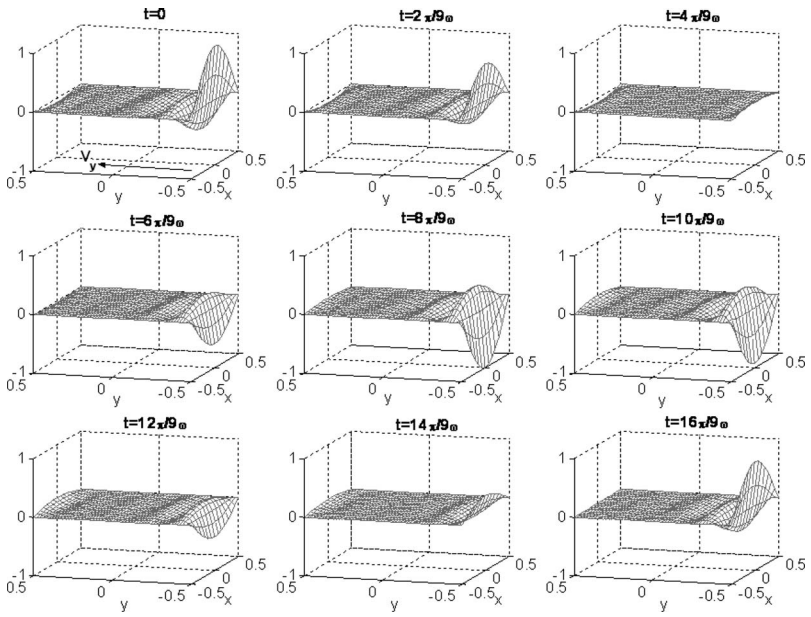

Fig. 15 First flutter mode shape for $\varepsilon = 5 \times 10^{-6}$, $\Lambda = 40$, $c = V_x = 0$, V_y nonzero. Nine time instances during 1 cycle of oscillation are shown.

changed" following the veering as shown in Figs. 14(*c*) and 14(*d*). Figures 14(*c*) and 14(*d*) show the real parts of the eigenfunctions at Points *C* and *D* in Fig. 14(*a*) and clearly show that the 08 basis function dominates these eigenfunctions. The higher order mode frequencies rapidly decrease as the cross-span flow velocity increases and approach the 00 mode frequency, and many eigenvalue loci veer before initial divergence instability (see inset of Fig. 14(*a*)). Figures 14(*e*) and 14(*f*) again show eigenfunctions before and after veerings, indicating that the 08 basis function dominates the first divergence mode shape by successively veering with all the lower order modes as cross flow is increased. As discussed in Ref. [22], that the loci indeed veer can be verified by performing a convergence study (with respect to the number of basis functions included in the discretization) of the coupling factors between two veering modes in the neighborhood of the veering.

The onset of flutter due to cross flow occurs with zero frequency at $V_y = 0.0693$, with a very high number of nodes in the cross-span direction and with high vibration localization at the leading edge. The first flutter mode shape is plotted in Fig. 15, clearly demonstrating the complex spatial pattern in the cross-span direction and also demonstrating vibration localization at the leading edge of the web due to the coalescence of modes that are largely symmetric and antisymmetric in the cross-span direction. As the flow speed is increased further past $V_y = 0.0693$, these two modes diverge and coalesce, leading to flutter with vanishing flutter frequency. As the flow speed is further increased, several other modes diverge and flutter. Interestingly, as ε is further decreased, even higher order modes will diverge first and the flutter vibration localization at the leading edge becomes even more pronounced.

The stability boundaries of the web as a function of the bending stiffness to tension ratio ε and the cross machine direction air flow V_y are shown in Fig. 16. As ε decreases, the divergence and subsequent flutter instability occur at lower air flow velocities. Moreover, at certain combinations of flow speed V_y and ε, the divergence and flutter points coincide, leading the possibility of rich postflutter dynamics near such degenerate points. The stability boundaries display apparent nonsmoothness at certain parameter values. These correspond to ε and V_y values beyond which a mode other than the 08 mode destabilizes first. Typically, as ε decreases, the cross-span modes that destabilize at lowest cross flow speed correspond to higher cross-span nodal number modes.

Note that no results have been presented on the stability in the presence of both web transport and cross machine flow. This is because of the prohibitively large number of basis functions needed for such computations. However, based on the present results, it is anticipated that for low web transport speeds, (a) web transport reduces the critical cross flow speed required for instability, because subcritical transport speeds reduce web frequencies and (b) the unstable vibrations with web transport and cross machine flow will feature phase propagation along both the *X* and the *Y* axes.

6 Effects of Dissipation

Dissipation in axially moving webs can arise from a number of sources including web material damping, roller elasticity, and fluid viscosity and boundary layer effects. It is worth noting that there have been no reported studies in literature of damping mechanisms for axially moving material problems. Accordingly, two general damping models will be discussed here: first, ground fixed damping only ($C_a \neq 0, C_w = 0$); second, comoving damping ($C_a = 0$, $C_w \neq 0$, see Eq. (1)).

If the effects of dissipation are modeled by ground fixed damping only, a positive definite damping matrix $\mathbf{C}_1$ arises in the discretized dynamical system (Eq. (15)). The theorems of Kelvin, Tait, and Chetaev (KTC) on dissipation induced destabilization of gyroscopic systems [23] are directly applicable to this problem. For the cases involving axial web transport and machine direction fluid flow, web flutter occurs through mode coalescence following gyroscopic restabilization. In these cases, the KTC theorem predicts that the system destabilizes upon initiation of gyroscopic restabilization. However, the divergence instability limits will remain unchanged. Moreover, because gyroscopic restabilization occurs between flow or transport speeds that lie between divergence and flutter speeds, the speed at which dissipation induced destabilization occurs is tightly bounded between the divergence and flutter speeds. In this sense, the instability boundaries predicted for the undamped system are only slightly affected upon addition of ground fixed damping. Moreover, for the cross-machine direction flow case, because no gyroscopic stabilization

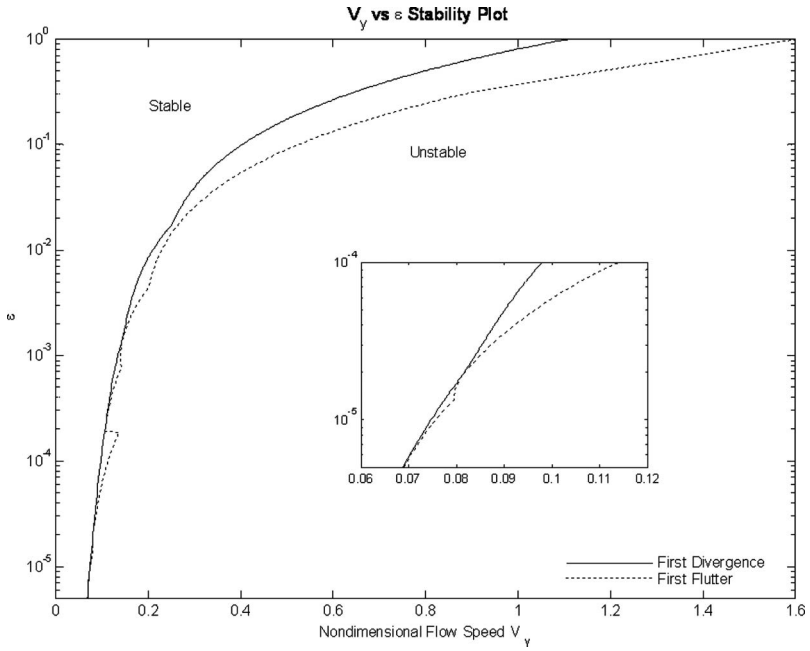

Fig. 16 First occurrence of divergence and flutter as bending stiffness to tension ratio ε and nondimensional cross flow V_y are varied

occurs in the initial instability, the instability limits and mode shapes will remain unaffected by this form of dissipation.

On the other hand, web material damping is best modeled as a comoving damping defined as a combination of positive definite damping and circulatory terms $C_w(u_{,t}+cu_{,x})$, where $C_w \neq 0$ in Eq. (1). In the absence of any form of damping, the system eigenvalues are symmetrically placed with respect to the origin of the complex plane. It can be shown that upon the presence of a comoving damping alone, the system essentially becomes quasi-Hamiltonian, with the eigenvalues symmetrically placed with respect to the point $-C_w/2+0i$ in the complex plane. For the cases of (a) stationary and axially moving web coupled to machine direction flow and (b) stationary web coupled to cross machine flow, the presence of small comoving damping only slightly modifies the divergence and flutter instability limits. This is because for small damping, the unstable eigenvalues now need to overcome an initially negative real part $-C_w/2$ before destabilizing the system. For the axially moving web coupled to an initially quiescent flow, the positive real parts of the eigenvalues resulting in instability are very small ($O(10^{-4})$), although they become larger as higher order modes flutter within a very small speed range (see Fig. 8). Thus, the addition of small comoving damping may suppress divergence and delay flutter of the lower modes, causing the initial instability to occur in a mode with higher number of nodes in the X direction. However, because the divergence and flutter speeds of a number of modes are tightly clustered together at supercritical speed, the overall divergence and flutter speed will only slightly increase, and the unstable mode is likely to possess larger number of nodes in the X direction.

In the presence of both stationary and comoving damping, it is expected that divergence and flutter speeds lie in between those predicted for stationary damping alone and for comoving damping alone. In this sense, the predictions of instability boundaries for undamped webs are quite robust with respect to unmodeled dissipative effects.

7 Comparison to Previous Results in Literature

The reduction in modal frequency caused by the addition of an initially quiescent potential flow has been shown by various authors. Niemi and Pramila [17] use the FEM to analyze a web span with a similarly small bending stiffness to tension ratio, twice as long with much smaller aspect ratio ($\kappa=0.2$) than the web system considered in this work. Their FEM results show that the 00 stationary web modal frequency is reduced to 25% of its in vacuo value, the 01 mode to 49% and the 02 mode to 54%. The 00 modal frequency was experimentally measured by Pramila [14,15] and shown to be 21–24% of its in vacuo value. This work predicts that the 00 modal frequency is reduced to 21% of its in vacuo value, 01 mode to 27%, and 02 mode to 32%. Raman et al. [6] measured the frequencies, gain, and phase of the vibrations of a stationary paper web excited by loudspeaker. Their work considered a shorter web with smaller aspect ratio, so the air coupling frequency reduction is less pronounced. The experiments show that the 00 modal frequency reduced to 46% of its in vacuo value, and the 01 mode to 61%. Pramila [14,15] also collected vibration measurements on an axially moving web at up to 20% of the critical transport speed and showed that the lowest frequency is slightly reduced at low transport speeds. This behavior is similar to the predictions shown here in Fig. 7.

Raman et al. [6] experimentally measured by using acoustic excitation from a speaker the mode shapes of a stationary, tensioned paper web coupled to surrounding air. Their experiments clearly indicate that the vibration amplitude at the web edges is significantly reduced compared to the theoretical in vacuo predictions. Indeed, the 00 and 01 mode shapes of the air-coupled web predicted in this work (Figs. 6(*b*) and 6(*d*)) are remarkably similar to the experimental ones measured by Raman et al. [6] and exhibit the same characteristic small amplitude at the free edges.

Watanabe et al. [9] and Chang and Moretti [11] investigated flutter of stationary webs due to cross flow. In both works, the paper webs considered had characteristically small bending stiffness to tension ratios, and in both works, the cross-span flutter mode shape is extremely wavy. Photographs of the cross-span flutter mode from Ref. [9] show approximately five half waves. The theoretical predictions in the preceding sections also predict the divergence and flutter of a very high nodal line cross-span mode. However, a direct comparison of flutter mode shapes is not possible, since in Ref. [9] the web was covered by a fairing at the leading edge and in Ref. [11] the web was clamped at the leading edge.

Watanabe et al. [9] developed an equation from experimental results to predict the first flutter cross flow speed. They describe the following relationships: The first flutter cross flow speed decreases as the bending stiffness decreases, as the tension decreases, as the air density increases, and as the web length increases. Chang and Moretti [11] also show that the first flutter cross flow speed decreases as the tension decreases. All of these general relationships between the first flutter cross flow speed and the web system parameters are in good agreement with the results in this paper. Recall from Eq. (7) that the bending stiffness to tension ratio is $\varepsilon = D/(a^2 N_{xx})$, the nondimensional flow speed is $V_y' = V_y/(N_{xx}/\rho)^{-1/2}$, and the fluid density parameter is $\Lambda = \rho_{air} a/\rho$ (the primes denoting nondimensional variables that have been dropped in previous sections are included in this paragraph). Figure 16 demonstrates that the nondimensional cross flow $(V_y/(N_{xx}/\rho)^{-1/2})$ first flutter speed decreases as the bending stiffness to tension ratio $(D/(a^2 N_{xx}))$ decreases, clearly confirming that the first flutter speed decreases with decreasing bending stiffness and increasing web span length. Since tension is a parameter in both ε and V_y', it is not immediately clear how tension affects the flutter speed, but further numerical investigations confirmed that the first flutter speed decreases with decreasing tension. The decrease in the first flutter flow speed per decrease in tension becomes more pronounced when higher order cross-span modes lose stability first. Recall also that for the stationary web in cross flow, the overall stiffness matrix loses stability through the $2\Lambda V_y'^2 \mathbf{K}_{\text{air2}}$ component, so an increase in $\Lambda = \rho_{air} a/\rho$ decreases the critical cross flow speed and the first flutter cross flow speed. The stability trends of a stationary web in cross flow predicted here therefore are qualitatively well supported by literature. However, because existing literature has focused on thin films supported on one edge, new experiments are needed to satisfactorily verify the predictions in this work.

8 Conclusions

The stability of the transverse vibrations of a uniaxially tensioned, axially moving plate of finite width coupled to initially quiescent and initially moving incompressible flows, at subcritical and supercritical speeds, is investigated in detail. A semianalytical method using FEM for the fluid coupling and the assumed modes method for the moving web is developed for this purpose. The main results of the study are as follows.

1. The out-of-plane, linear vibrations of an axially moving web coupled to initially moving base flows of an incompressible fluid can be modeled as a discretized, undamped gyroscopic dynamical system with a symmetric stiffness matrix. The inclusion of ground fixed and comoving damping adds positive definite damping and circulatory terms to the dynamical system.
2. In vacuum, the web modal frequencies cluster together around those of an equivalently tensioned string. At a supercritical transport speed, the axially moving web undergoes divergence instability and gyroscopic restabilization, and several modes coalesce and flutter within a very small speed range.
3. Web vibration coupling to an initially quiescent potential flow significantly reduces the web frequencies, spreads apart the frequency clusters, and considerably reduces the free edge displacement in every stationary web mode shape. While the critical transport speed and speed for gyroscopic restabilization remain unchanged, the supercritical flutter speed and frequency are slightly reduced air density to web density ratio considered here.
4. Addition of an axial flow V_x equal to the web transport speed significantly lowers the critical transport speed and flutter speed. Free edge displacements of the unstable vibrations are also reduced. Upon flow reversal $V_x \rightarrow -V_x$, the transport critical speed remains unchanged but the flutter speeds decrease. For all the cases above, the initial instability occurs through the coalescence of the 00 and 10 modes.
5. Upon inclusion of a cross machine flow, however, modes with several nodes in the cross-span direction diverge first at very small values of cross flow speed V_y. The first flutter mode shape is very "wavy" with significant localization of the unstable vibration at the leading edge. Furthermore, the onset of flutter occurs through mode coalescence on the real axis with zero flutter frequency.
6. The effects of ground fixed and comoving damping on the web instability mechanisms are also discussed. In the presence of ground fixed damping alone, the web generally destabilizes via a classical double-zero eigenvalue stability as predicted by the KTC theorem. However, the web stability boundaries differ very little from those found for flutter via mode coalescence for undamped webs. Moreover, the instability mechanisms and boundaries due to the cross flow remain unaffected upon inclusion of ground fixed damping. Comoving damping does not significantly alter the instability mechanisms for most cases considered here. However, for the case of an axially moving web coupled to an initially quiescent flow, the presence of comoving damping alters the unstable mode to one with higher nodes in the X direction. The overall transport speed for flutter is only slightly modified.
7. Several predicted results and phenomena are compared to existing experimental results in literature and are found to qualitatively match. However, several experimental conditions are different from those considered in this model, and new experiments need to be performed to quantitatively verify the predicted results.

In several cases considered, the typically small bending stiffness to tension ratio of tensioned webs plays a key role in the occurrence of a cascade of divergence, gyroscopic restabilizations, and flutter over an extremely small web transport speed. While the linear stability analysis presented in this paper is sufficient to predict the onset of such instabilities, in reality, it is expected that the resulting unstable flutter motions comprise of several web modes exhibiting very complex spatiotemporal dynamics. Moreover, the inclusion of leading or trailing edge wake effects for the cross machine flow problem could introduce additional nonconservative terms compared to the idealized fluid model considered here. Clearly, a better understanding of web flutter, especially postflutter dynamics, requires the inclusion of wake effects, membrane geometric nonlinearities, and nonlinear boundary conditions at the fluid-web interface. These are the topics of ongoing research by the authors.

Acknowledgment

The corresponding author (A.R.) gratefully acknowledges financial support for this research from the National Science Foundation (CAREER, NSF 0134455-CMS) and from the author's group of industrial sponsors. The first author (M.V.) was partly supported through the John and Helen Lozar and the Winkleman Fellowships at Purdue University.

Appendix

The components of the matrices of the discretized system (15) are as follows:

$$(M_{\text{air}})_{ij;mn} = \int_{x=-0.5}^{0.5} \int_{y=-\kappa/2}^{+\kappa/2} \psi_{ij}(x,y)\varphi_{mn3}(x,y,0^+)dxdy$$

$$(G)_{ij;mn} = \int_{x=-0.5}^{0.5} \int_{y=-\kappa/2}^{+\kappa/2} \psi_{ij}(x,y)\psi_{mn,x}(x,y)dxdy$$

$$(G_{\text{air }1})_{ij;mn} = \int_{x=-0.5}^{0.5} \int_{y=-\kappa/2}^{+\kappa/2} \psi_{ij}(x,y)[\varphi_{mn1}(x,y,0^+) + \varphi_{mn3,x}(x,y,0^+)]dxdy$$

$$(G_{\text{air }2})_{ij;mn} = \int_{x=-0.5}^{0.5} \int_{y=-\kappa/2}^{+\kappa/2} \psi_{ij}(x,y)[\varphi_{mn2}(x,y,0^+) + \varphi_{mn3,y}(x,y,0^+)]dxdy$$

$$(K_1)_{ij;mn} = \int_{x=-0.5}^{0.5} \int_{y=-\kappa/2}^{+\kappa/2} \psi_{ij,x}(x,y)\psi_{mn,x}(x,y)dxdy$$

$$(K_2)_{ij;mn} = \int_{x=-0.5}^{0.5} \int_{y=-\kappa/2}^{+\kappa/2} \{\psi_{ij,xx}(x,y)\psi_{mn,xx}(x,y) + \psi_{ij,yy}(x,y)\psi_{mn,yy}(x,y) + 2(1-\mu)\psi_{ij,xy}(x,y)\psi_{mn,xy}(x,y) + \mu[\psi_{ij,xx}(x,y)\psi_{mn,yy}(x,y) + \psi_{ij,yy}(x,y)\psi_{mn,xx}(x,y)]\}dxdy$$

$$(K_{\text{air }1})_{ij;mn} = \int_{x=-0.5}^{0.5} \int_{y=-\kappa/2}^{+\kappa/2} \psi_{ij}(x,y)\varphi_{mn1,x}(x,y,0^+)dxdy$$

$$(K_{\text{air }2})_{ij;mn} = \int_{x=-0.5}^{0.5} \int_{y=-\kappa/2}^{+\kappa/2} \psi_{ij}(x,y)\varphi_{mn2,y}(x,y,0^+)dxdy$$

$$(K_{\text{air }3})_{ij;mn} = \int_{x=-0.5}^{0.5} \int_{y=-\kappa/2}^{+\kappa/2} \psi_{ij}(x,y)[\varphi_{mn1,y}(x,y,0^+) + \varphi_{mn2,x}(x,y,0^+)]dxdy$$

$$(C_1)_{ij;mn} = \int_{x=-0.5}^{0.5} \int_{y=-\kappa/2}^{+\kappa/2} \psi_{ij}(x,y)\psi_{mn}(x,y)dxdy$$

$$(C_2)_{ij;mn} = \int_{x=-0.5}^{0.5} \int_{y=-\kappa/2}^{+\kappa/2} \psi_{ij}(x,y)\psi_{mn,x}(x,y)dxdy$$

References

[1] Ulsoy, A. G., and Mote, C. D., Jr., 1982, "Vibration of Wide Band-Saw Blades," ASME J. Eng. Ind., **104**, pp. 71–78.

[2] Wang, X., 1999, "Numerical Analysis of Moving Orthotropic Thin Plates," Comput. Struct., **70**, pp. 467–486.

[3] Laukkanen, J., 2002, "FEM Analysis of a Travelling Web," Comput. Struct., **80**, pp. 1827–1842.

[4] Koivurova, H., and Pramila, A., 1997, "Nonlinear Vibration of Axially Moving Membrane by Finite Element Method," Comput. Mech., **20**, pp. 573–581.

[5] Mockensturm, E. M., and Mote, C. D., Jr., 1999, "Steady Motions of Translating, Twisted Webs," Int. J. Non-Linear Mech., **34**, pp. 247–257.

[6] Raman, A., Wolf, K. D., and Hagedorn, P., 2001, "Observations on the Vibrations of Paper Webs," *Proceedings of the International Conference on Web Handling*, Stillwater, OK.

[7] Guo, C. Q., and Paidoussis, M. P., 2000, "Stability of Rectangular Plates With Free Side-Edges in Two-Dimensional Inviscid Channel Flow," ASME J. Appl. Mech., **67**(1), pp. 171–176.

[8] Hill, K. C., 1988, "Dryer Sheet Stability for Older Paper Machines," Tappi J., **71**, pp. 55–59.

[9] Watanabe, Y., Suzuki, S., Sugihara, M., and Sueoka, Y., 2002, "An Experimental Study of Paper Flutter," J. Fluids Struct., **16**(4), pp. 529–542.

[10] Chang, Y. B., and Moretti, P. M., 1992, "An Experimental Study on Edge Flutter in Webs," *Applied Mechanics Division-Proceedings of the ASME*, Vol. 149.

[11] Chang, Y. B., and Moretti, P. M., 2002, "Flow-Induced Vibration of Free Edges of Thin Films," J. Fluids Struct., **16**(7), pp. 989–1008.

[12] Chang, Y. B., Cho, H. C., and Moretti, P. M., 1999, "Edge Flutter," *Noise Control and Acoustics Division-Proceedings of the ASME*, Vol. 26, pp. 413–423.

[13] Watanabe, Y., Isogai, K., Suzuki, S., and Sugihara, 2002, M., "A Theoretical Study of Paper Flutter," J. Fluids Struct., **16**(4), pp. 543–560.

[14] Pramila, A., 1986, "Sheet Flutter and the Interaction Between Sheet and Air," Tappi J., **69**, pp. 70–74.

[15] Pramila, A., 1987, "Natural Frequencies of a Submerged Axially Moving Band," J. Sound Vib., **113**, pp. 198–203.

[16] Wang, X., 1997, "Finite Element Analysis of Air-Sheet Interactions and Flutter Suppression Devices," Comput. Struct., **64**(5/6), pp. 983–994.

[17] Niemi, J., and Pramila, A., 1987, "FEM-Analysis of Transverse Vibrations of an Axially Moving Membrane Immersed in Ideal Fluid," Int. J. Numer. Methods Eng., **24**, pp. 2301–2313.

[18] Turnbull, P. F., Perkins, N. C., and Schultz, W. W., 1995, "Contact-Induced Nonlinearity in Oscillating Belts and Webs," J. Vib. Control, **1**, pp. 459–479.

[19] Lamb, H., 1932, *Hydrodynamics*, Dover, New York, pp. 6–8.

[20] Katz, J., and Plotkin, A., 2001, *Low Speed Aerodynamics*, Cambridge University Press, Cambridge.

[21] Meyerhoff, W. K., 1970, "Added Masses of Thin Rectangular Plates Calculated From Potential Theory," J. Ship Res., **14**, pp. 100–111.

[22] Perkins, N. C., and Mote, C. D., 1986, "Comments on Curve Veering in Eigenvalue Problems," J. Sound Vib., **106**(3), pp. 451–463.

[23] Merkin, D. R., 1997, *Introduction to the Theory of Stability*, Springer, New York, pp. 181–196.